Journal of Colloid and Interface Science 644 (2023) 10–18

Contents lists available at ScienceDirect

Journal of Colloid And Interface Science

journal homepage: www.elsevier.com/locate/jcis

# Multilevel spatial confinement of transition metal selenides porous microcubes for efficient and stable potassium storage

Rui Zhang [a,1], Qing Luo [a,1], Juan Gong [a,1], Zhikun Chen [a], Zhuang Wu [a], Shiman Li [a], Qiaoji Zheng [a,*], Xiaochun Wu [a], Kwok-ho Lam [b,*], Dunmin Lin [a,*]

[a] College of Chemistry and Materials Science, Sichuan Normal University, Chengdu 610066, PR China
[b] Centre for Medical and Industrial Ultrasonics, James Watt School of Engineering, University of Glasgow, Glasgow, Scotland, United Kingdom

## GRAPHICAL ABSTRACT

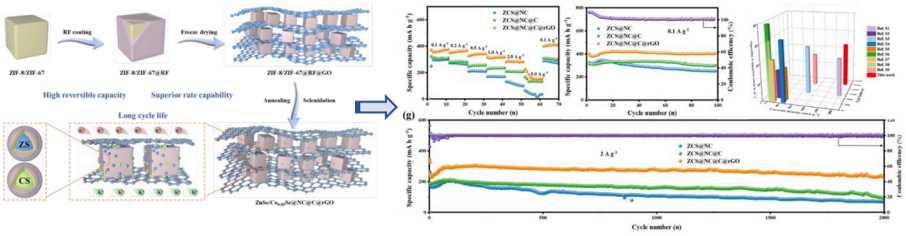


## ARTICLE INFO

*Keywords:*
Potassium-ion batteries
Bimetallic selenides
Multilevel spatial confinement
Bimetal MOFs

## ABSTRACT

Recently, potassium-ion batteries (PIBs) have been considered as one of the most promising energy storage systems; however, the slow kinetics and large volume variation induced by the large radius of potassium ions ($K^+$) during chemical reactions lead to inferior structural stability and weak electrochemical activity for most potassium storage anodes. Herein, a multilevel space confinement strategy is proposed for developing zinc-cobalt bimetallic selenide ($ZnSe/Co_{0.85}Se$@NC@C@rGO) as high-efficient anodes for PIBs by *in-situ* carbonizing and subsequently selenizing the resorcinol–formaldehyde (RF)-coated zeolitic imidazolate framework-8/zeolitic imidazolate framework-67 (ZIF-8/ZIF-67) encapsulated into 2D graphene. The highly porous carbon microcubes derived from ZIF-8/ZIF-67 and carbon shell arising from RF provide rich channels for ion/electron transfer, present a rigid skeleton to ensure the structural stability, offer space for accommodating the volume change, and minimize the agglomeration of active material during the insertion/extraction of large-radius $K^+$. In addition, the three-dimensional (3D) carbon network composed of graphene and RF-derived carbon-coated microcubes accelerates the electron/ion transfer rate and improves the electrochemical reaction kinetics of the material. As a result, the as-synthesized $ZnSe/Co_{0.85}Se$@NC@C@rGO as the anode of PIBs possesses the excellent rate capability of 203.9 mA h $g^{-1}$ at 5 A $g^{-1}$ and brilliant long-term cycling performance of 234 mA h $g^{-1}$ after 2,000 cycles at 2 A $g^{-1}$. *Ex-situ* X-ray diffraction (*Ex-situ* XRD) diffraction reveals that the intercalation/de-intercalation of $K^+$ proceeds through the conversion-alloying reaction. The proposed strategy based on the spatial confinement engineering is highly effective to construct high-performance anodes for PIBs.

* Corresponding authors.
*E-mail addresses:* joyce@sicnu.du.cn (Q. Zheng), kwokho.lam@glasgow.ac.uk (K.-h. Lam), ddmd222@sicnu.edu.cn (D. Lin).
[1] These authors contributed equally to this work.

https://doi.org/10.1016/j.jcis.2023.04.035
Received 31 January 2023; Received in revised form 29 March 2023; Accepted 10 April 2023
Available online 11 April 2023

## 1. Introduction

In the past 20 years, lithium-ion batteries (LIBs) have extensively been used in electric vehicles, portable electronic devices, and other fields. However, the shortage and unbalanced geographical distribution of lithium resources limit the further sustainable application of lithium-based energy storage devices [1,2]. Recently, as one of the promising substitutes, potassium has attracted extensive attention due to the advantages of abundant resource, low cost, easy exploitation, suitable redox potential ($K^+$/K: −2.94 V vs SHE) and similar physical/chemical properties to lithium [3,4]. Besides, potassium-ion batteries (PIBs) possess relatively high operating voltage and good rate capability due to the weak Lewis acidity of potassium ions, low standard potential of $K^+$/K and high conductivity of potassium-based electrolytes [5,6]. However, the slow kinetics and large volume variation during chemical reactions induced by the large radius of $K^+$ would lead to inferior structural stability and weak electrochemical activity for most potassium-based anodes of storage devices [7–10]. Therefore, it is crucial to develop advanced anode materials for accommodating the embedding/de-embedding of large $K^+$.

Among various candidates of anode materials for PIBs, transition metal selenides (TMS) have gained much attention owing to their desirable theoretical capacity, low cost and good redox reversibility [11–14]. For example, Yu et al. synthesized the $CoSe_2$ nanoparticles immobilized in *N*-doped carbon nanotubes with a specific capacity of 253 mA h $g^{-1}$ at 0.2 A $g^{-1}$ after 100 cycles and a rate performance of 173 mA $g^{-1}$ at 2.0 A $g^{-1}$ when used as anodes for PIBs [15]. Wang et al. constructed the porous Mn-Fe-Se adhered/inserted with interlaced CNTs (denoted as Mn-Fe-Se/CNTs), and the material exhibits an excellent long term cycle stability of 141 mA h $g^{-1}$ after 70 cycles at 0.05 A $g^{-1}$ [16]. Nevertheless, most TMS materials still inevitably suffer from sluggish kinetics behavior and severe structural collapse/easy pulverization during the repeated insertion/extraction of large $K^+$, presenting poor electrochemical performance [17]. Obviously, designing anode materials with the ability to adopt the volume stress and ensure the structural integrity is the main challenge to achieve the high-performance potassium storage. Though nanosized active materials have been reported to effectively accelerate ion diffusion and alleviate volume stress during charging/discharging due to the short ion transport path and the full contact between electrolyte and active material, the nanoparticles are prone to agglomeration due to their high surface energy [18–20]. Fortunately, the strategy of space confinement engineering based on high-conductivity carbon materials with rich types has been demonstrated to address the issues of sluggish kinetics, agglomeration and structural collapse/pulverization of potassium-based anodes [21–23]. For example, Yang et al. fabricated $CoSe_2$@C as the anode material for PIBs, in which the carbon group effectively alleviates the volume expansion during the insertion/extraction of $K^+$, overcomes the particle agglomeration, and improves the stability of the electrode material [24]. Jia et al. prepared CuS nanosheets uniformly anchored on graphene oxide (CuS@GO), giving a specific capacity of 290.5 mA h $g^{-1}$ after 100 cycles at 0.1 A $g^{-1}$ [25]. Nevertheless, it is challenging for conducting a single level of carbon confinement engineering to achieve highly active redox behaviors for PIBs.

Herein, a multilevel spatial confinement strategy for zinc-cobalt bimetallic selenide (ZnSe/$Co_{0.85}$Se@NC@C@rGO) is proposed to synthesize high-efficient anodes for PIBs by *in-situ* carbonizing and selenizing the resorcinol–formaldehyde (RF)-coated ZIF-8/ZIF-67 encapsulated into two-dimensional (2D) graphene. This three-dimensional (3D) interconnected carbon network composed of *N*-doped carbon (NC), RF-derived carbon (C) and reduced graphene oxide (rGO) embedded with bimetallic selenides exhibits the following advantages: (1) compared with monometallic selenides, bimetallic selenide of ZnSe/$Co_{0.85}$Se is favored by the synergistic effect between ZnSe and $Co_{0.85}$Se, exhibiting more redox potential and higher electronic conductivity; (2) the highly porous carbon derived from ZIF-8/ZIF-67 provides the space with a certain volume margin for alleviating the volume stress induced by the repeated insertion/extraction of large potassium ions, presents rich channels for ion/electron transfer, and promotes the full penetration of electrolyte and the exposure of active sites for electrochemical reaction; [26] (3) the rigid skeleton arising from the coating layer of the RF ensures the structural integrity of anode material and avoids the structural collapse after long-term cycling; (4) the triple-carbon confinement strategy inhibits the agglomeration and pulverization of active nanoparticles, while the 3D network composed of graphene, porous carbon and RF-derived carbon shell accelerates the electron/ion transfer and promotes the electrochemical reaction kinetics. Consequently, the as-synthesized ZCS@NC@C@rGO composite exhibits excellent electrochemical properties: a high initial specific capacity of 863 mA h $g^{-1}$ at 0.1 A $g^{-1}$, an excellent rate capability of 203.9 mA h $g^{-1}$ at 5 A $g^{-1}$ and an outstanding long-term cycling performance of 234 mA h $g^{-1}$ after 2000 cycles.

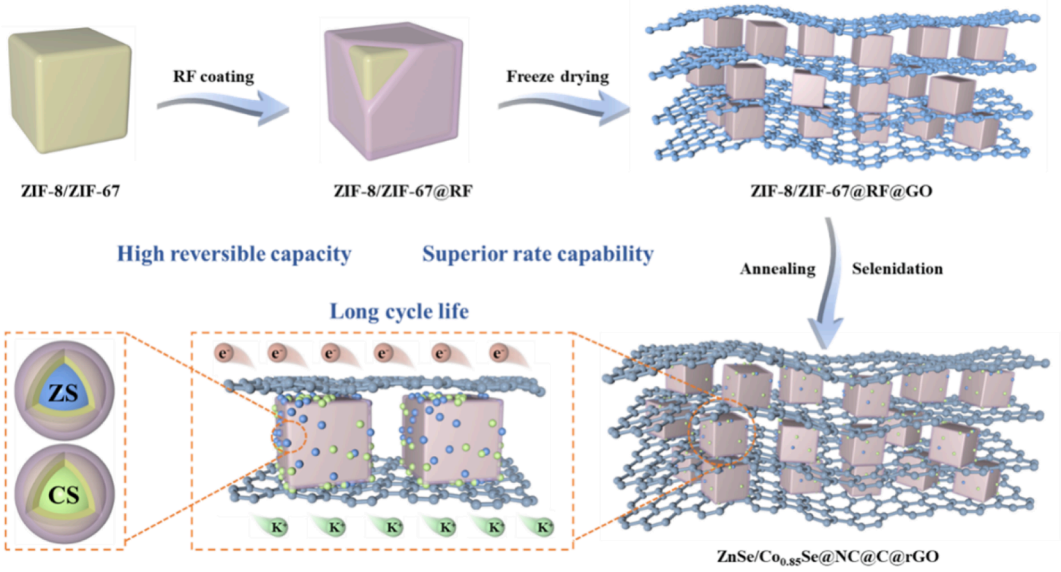


**Fig. 1.** Schematic illustration of the synthesis process of ZnSe/$Co_{0.85}$Se@NC@C@rGO composite.

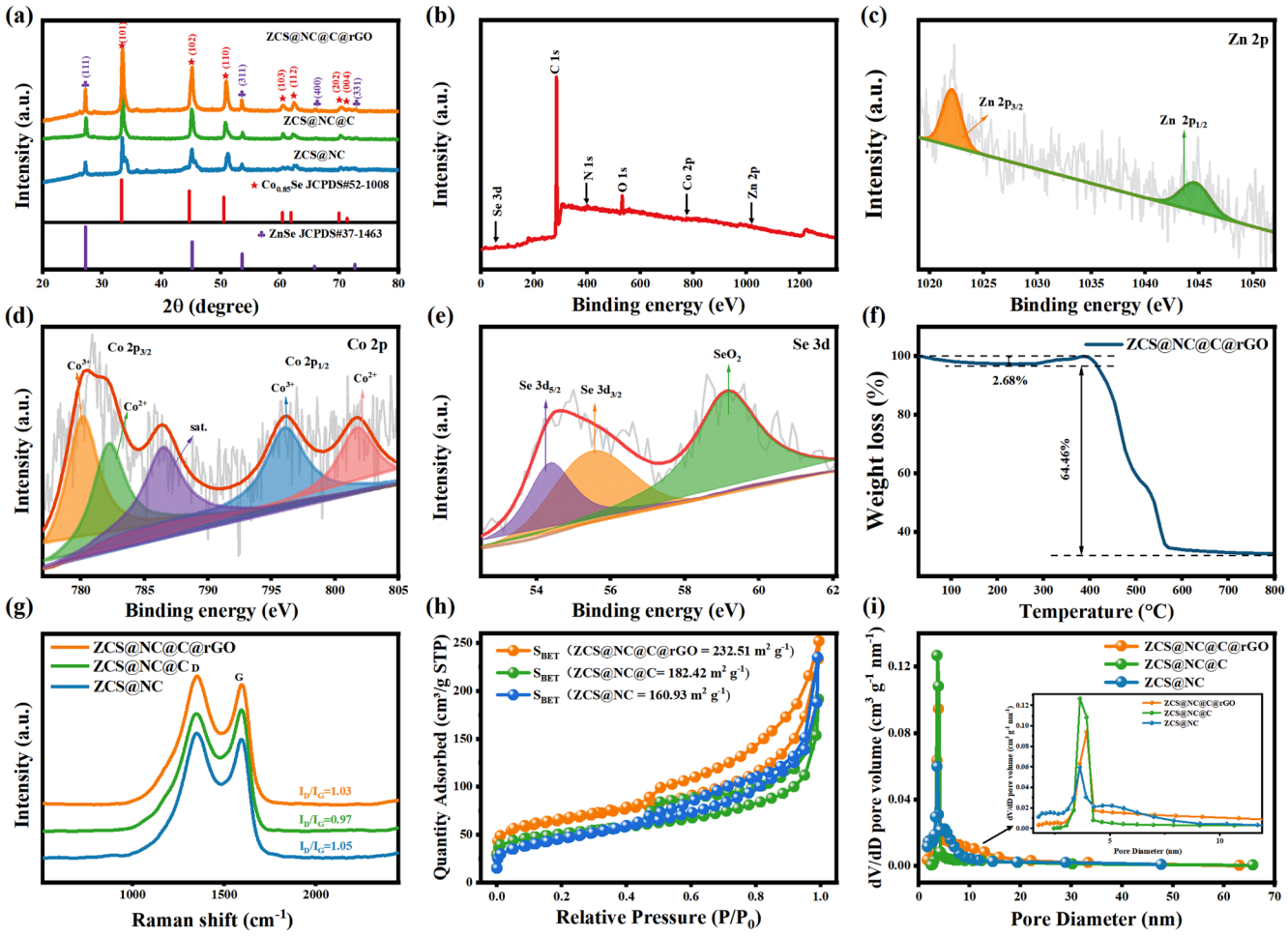


**Fig. 2.** (a) XRD patterns of ZCS@NC, ZCS@NC@C and ZCS@NC@C@rGO; (b) XPS spectrum of ZCS@NC@C@rGO; (c-e) High-resolution XPS spectra of (c) Zn 2p, (d) Co 2p and (e) Se 3d in ZCS@NC@C@rGO; (f) TGA profile of ZCS@NC@C@rGO; (g) Raman spectra of ZCS@NC, ZCS@NC@C and ZCS@NC@C@rGO; (h) Nitrogen adsorption desorption isotherms of ZCS@NC@C@rGO, ZCS@NC@C and ZCS@NC; (i) Pore size distributions of ZCS@NC@C@rGO, ZCS@NC@C and ZCS@NC.

## 2. Results and discussion

The synthesis process of the ZSC/NC@C@rGO composites is shown in Fig. 1. All experimental details are provided in Supporting Information. Firstly, the bimetallic MOFs microcubes of ZIF-8/ZIF-67 are synthesized by a simple co-precipitation method. Subsequently, RF polymer is uniformly coated on the surface of the ZIF-8/ZIF-67 microcubes (ZIF-8/ZIF-67@RF). After freeze-dried, the ZIF-8/ZIF-67@RF and graphene are cross-linked to form a 3D skeleton (ZIF-8/ZIF-67@RF@GO). Finally, the 3D network of the ZCS@NC@C@rGO is synthesized by *in-situ* carbonizing and selenizating the ZIF-8/ZIF-67@RF@GO.

The prepared ZIF-8/ZIF-67 microcrystals exhibit distinct diffraction peaks (Figure S1), which is consistent with the previous report [27]. Fig. 2a shows the powder X-ray diffraction (XRD) patterns of the ZNS@NC, ZCS@NC@C and ZCS@NC@C@rGO, where all the diffraction peaks are well indexed to the standard cards of ZnSe (JCPDS No. 37-1463) and $Co_{0.85}Se$ (JCPSD No. 52-1008). The X-ray photoelectron spectroscopy (XPS) is used to verify the chemical compositions and surface valence states of the ZCS@NC@C@rGO. From Fig. 2b, the elements of Zn, C, Se, C, N and O are detected in the ZCS@NC@C@rGO. The high-resolution Zn 2p spectrum in Fig. 2c shows two peaks at 1022 and 1045 eV, corresponding to $2p_{3/2}$ and $2p_{1/2}$ of Zn, respectively [28]. As shown in Fig. 2d, the two photoelectron peaks at 782.2 eV and 801.75 eV can be attributed to $Co^{2+}$ with Co $2p_{3/2}$ and Co $2p_{1/2}$, while the other two peaks at 780.25 and 796.04 eV can be ascribed to $Co^{3+}$ with Co $2p_{3/2}$ and Co $2p_{1/2}$, respectively [29,30]. The high-resolution Se 3d spectrum in Fig. 2e shows that the peaks at 54.36 and 55.5 eV can be assigned to Se $2d_{5/2}$ and Se $2d_{3/2}$, respectively; [31,32] and the peak at 59.13 eV may be related to Se-O, which can be attributed to the slight oxidation of the surface of the sample [33]. The fitting result of the high-resolution N 1s spectrum shows the presence of pyridine-like N (398.6 eV), pyrrole-like N (401.0 eV) and graphite-like N (403.5 eV) in the ZSC@NC@C@rGO (Fig. S2a), demonstrating the successful doping of nitrogen [34]. The introduction of N element not only accelerates the ion transport rate but also enhances the electron-donating capability of carbon microcubes. The C 1s spectrum of the ZCS@NC@C@rGO is shown in Fig. S2b. The peak at 283.6 eV is attributed to C═C, while the other two peaks are associated with C═N (284.8 eV) and C—N (286.2 eV), respectively [35,36]. The thermogravimetric analysis (TGA) result in Fig. 2f shows that the total content of carbon is 34.31% for the ZCS@NC@C@rGO. The Raman spectra of the ZCS@NC, ZCS@NC@C and ZCS@NC@C@rGO in Fig. 2g show two peaks at 1350 and 1594 $cm^{-1}$, which are the characteristic peaks of $sp^3$ hybridized disordered carbon (D band) and $sp^2$ hybridized graphitic carbon (G band) [37], respectively. As shown in Fig. 2h, the adsorption/desorption isotherm of $N_2$ for the ZCS@NC@C@rGO shows a typical type-IV curve with $H_2$ hysteresis loop [38], exhibiting rich mesopores (Fig. 2i). Meanwhile, the ZCS@NC@C@rGO shows a very large Brunauer-Emmett-Teller (BET) specific surface area of 232.51 $m^2\ g^{-1}$, which is much larger than that of the ZCS@NC@C (182.42 $m^2\ g^{-1}$) and ZCS@NC (160.93 $m^2\ g^{-1}$). Fig. 2i shows that the ZCS@NC, ZCS@NC@C and ZCS@NC@C@rGO all have abundant pore structures. The rich pore system and large specific surface

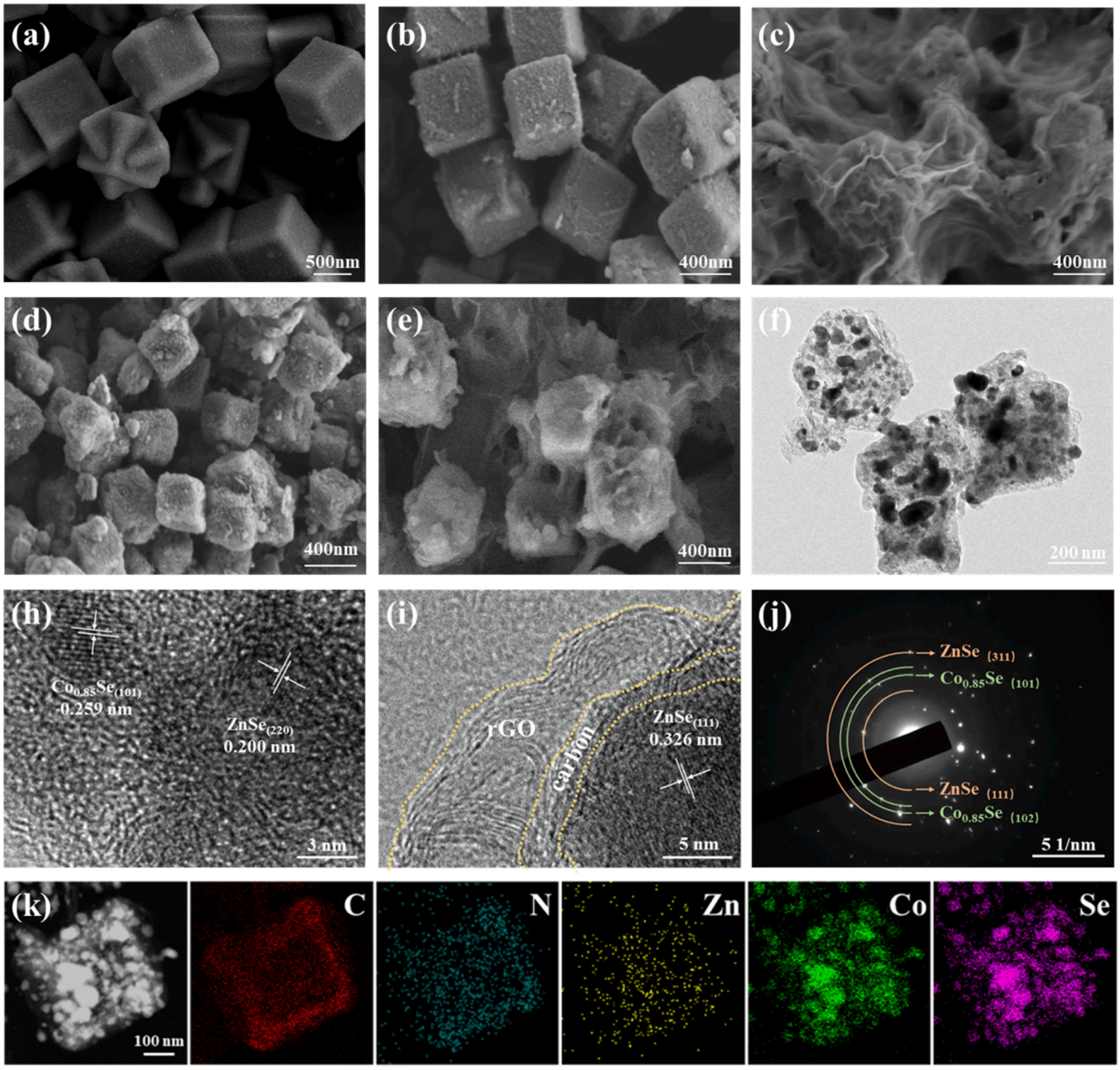


**Fig. 3.** Morphology and microstructure characterizations: SEM images of (a) ZIF-8/ZIF-67, (b) ZIF-8/ZIF-67@RF, (c) ZIF-8/ZIF-67@RF@GO, (d) ZCS@NC@C, (e) ZCS@NC@C@rGO; (f) TEM image, (h, i) HRTEM images, (j) SAED image, and (k) elemental mapping images of ZCS@NC@C@rGO.

of the ZCS@NC@C@rGO provide a buffering effect to mitigate the volume expansion during the $K^+$ embedding/de-embedding and present more active sites for the migration of $K^+$.

Fig. 3a-d show the scanning electron microscopy (SEM) images of the precursors and as-fabricated materials. As shown in Fig. 3a, the ZIF-8/ZIF-67 nanoparticles possess smooth surface and uniform particle sizes with an average size of 350 nm. In Fig. 3b, after coated with RF, the morphology of the ZIF-8/ZIF-67 is well maintained, but the surface becomes slightly rough. Fig. 3c demonstrates that the ZIF-8/ZIF-67@RF microcubes have been encapsulated into 2D graphene foam via the freeze-drying technique. After the annealing and selenization treatments (Fig. 3d and 3e), the materials become slightly small, but their morphologies are still well-maintained. In contrast, the ZCS@NC exhibits the irregular morphology (Fig. S3a). Obviously, the RF-derived carbon layer provides a rigid skeleton to avoid the structural collapse of the material during high-temperature treatments. The transmission electron microscopy (TEM) images of the ZCS@NC@C@rGO are shown in Fig. 3f and S3b. From the high-resolution TEM images (Fig. 3h and 3i), the lattice stripe spacings of 0.259 nm and 0.200 nm are well attributed to the (1 0 1) plane of $Co_{0.85}Se$ and the (2 2 0) plane of ZnSe, respectively. It can be seen that the ZnSe/$Co_{0.85}Se$ nanoparticles are uniformly encapsulated into a double-shell carbon consisting of *N*-doped carbon derived from the ligand of ZIF-8/ZIF-67 and RF-derived carbon, while ultrathin graphene sheets are uniformly covered on the surface of the microcubes. The selected area electron diffraction (SAED) pattern (Fig. 3j) reveals the polycrystalline features of the ZCS@NC@C@rGO, where two diffraction rings well match with the (1 0 2) and (1 0 2) crystallographic planes of $Co_{0.85}Se$, and the other two rings correspond to the (3 1 1) and (1 1 1) crystallographic planes of ZnSe. The element mapping images and energy dispersive X-ray (EDX) spectrum of the ZCS@NC@C@rGO demonstrate that the elements of C, N, Zn, Co and Se are uniformly distributed in the ZCS@NC@C@rGO composites (Fig. 3k and S4).

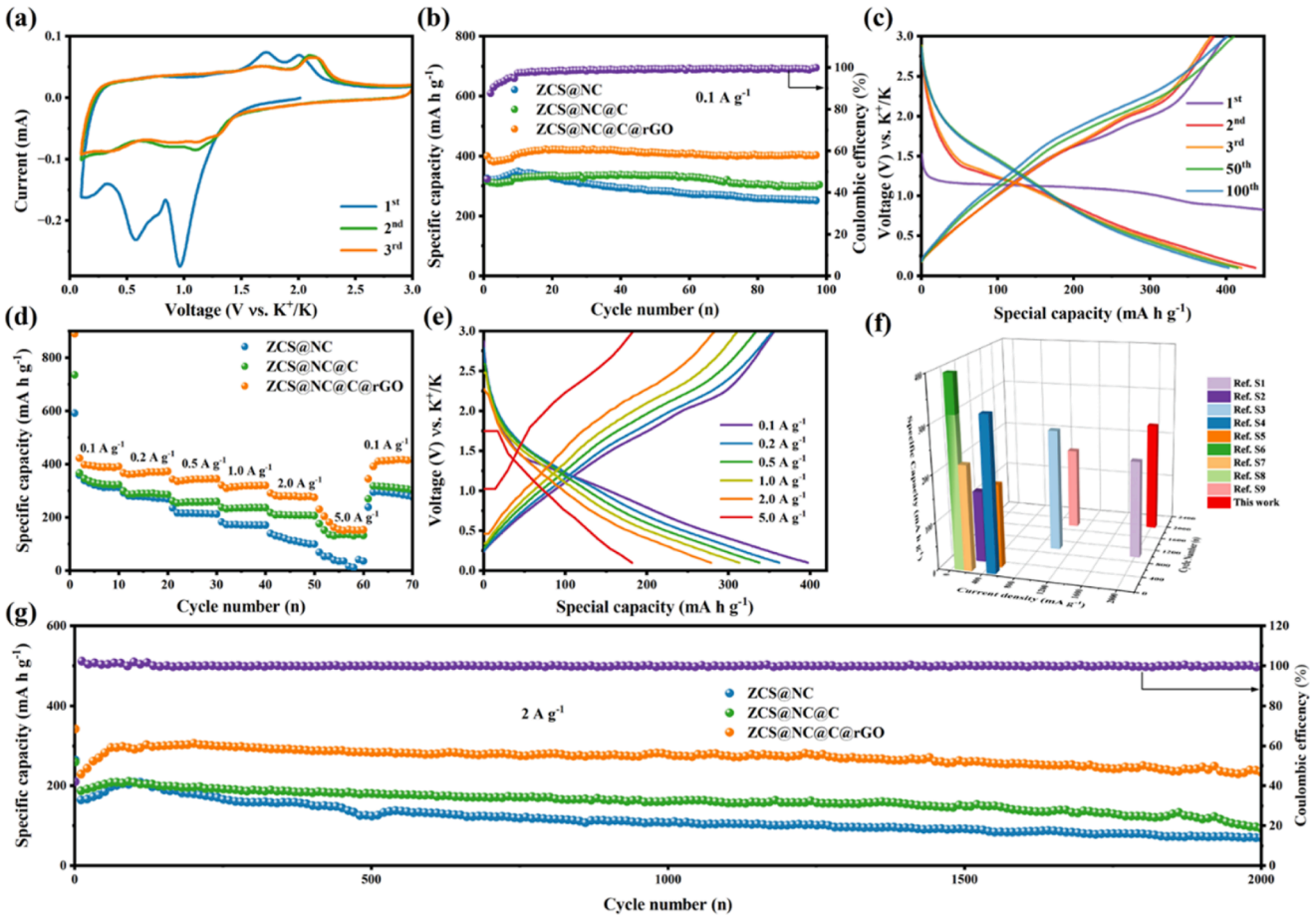


**Fig. 4.** (a) CV profiles of ZCS@NC@C@rGO at 0.1 mV $s^{-1}$; (b) Cyclic performance of ZCS@NC, ZCS@NC@C and ZCS@NC@C@rGO at 0.1 A $g^{-1}$; (c) Galvanostatic discharge/charge curves of ZCS@NC@C@rGO at 0.1 A $g^{-1}$; (d) Rate properties of ZCS@NC, ZCS@NC@C and ZCS@NC@C@rGO between 0.1 and 5 A $g^{-1}$; (e) Galvanostatic discharge/charge curves of ZCS@NC@C@rGO at different current densities; (f) Comparison of the electrochemical performance of ZCS@NC@C@rGO with the reported advanced anodes; and (g) Long-term cycling curves of ZCS@NC, ZCS@NC@C and ZCS@NC@C@rGO at 2 A $g^{-1}$.

To demonstrate the advantages of the ZCS@NC@C@rGO as the anode material for PIBs, the electrochemical properties of the ZCS@NC, ZCS@NC@C and ZCS@NC@C@rGO are evaluated and the results are shown in Fig. 4. The cyclic voltammetry profiles of the ZCS@NC@C@rGO for the first three cycles at 0.1 mV $s^{-1}$ in the voltage range of 0.1–3.0 V are presented in Fig. 4a. In the first cathodic scan, a distinct cathodic peak is observed at 0.956 V and disappears in the subsequent cycles, which can be ascribed to the formation of a stable solid-electrolyte interphase (SEI) film on the electrode surface. The smaller peak in the range of 0.9 to 0.1 V corresponds to the reactions related to the reduction of ZnSe to the Zn metal and the further alloying of Zn to $KZn_{13}$ and the conversion of $Co_{0.85}Se$ to Co metal. Similarly, in the first anodic scan, an oxidation peak appears at 1.704 V, which is associated with the dealloying of $KZn_{13}$ to form Zn and the reaction of Zn with $K_2Se$ to form ZnSe, while the oxidation peak at 1.998 V corresponds to the recovery of $Co_{0.85}Se$ from Co metal and $K_2Se$. [35,39,40,44] In the subsequent second and third cathodic scans, the cathodic peak shifts to higher potential, which may be due to the electrochemical activation process. In addition, the second and third CV curves of the ZCS@NC@C@rGO are highly coincident, indicating good reversibility of the active material. Fig. 4b shows the cyclic performance of the ZCS@NC, ZCS@NC@C and ZCS@NC@C@rGO at 0.1 A $g^{-1}$. Obviously, the ZCS@NC@C@rGO exhibits much better cyclic performance than the other two electrodes, delivering the large capacity of 402.5 mA h $g^{-1}$ after 100 charge/discharge cycles (ZCS@NC: 250.5 mA h $g^{-1}$; ZCS@NC@C: 298.4 mA h $g^{-1}$). Fig. 4c shows the charge/discharge curves of ZCS@NC@C@rGO at the 2nd, 3rd, 50th and 100th cycles, while the charge/discharge curves of the ZCS@NC and ZCS@NC@C are displayed in Fig. S5a and S5b, respectively. The curves in Fig. 4c show smooth slopes, which is consistent with the redox behavior in the CV results. Fig. 4d shows the rate performance of the three electrodes. For the ZCS@NC@C@rGO, the specific capacities of 422.2, 361.3, 335.2, 308.7, 281.7 and 203.9 mA h $g^{-1}$ are observed at 0.1, 0.2, 0.5, 1, 2 and 5 A $g^{-1}$, respectively, while the capacity is recovered to 408.4 mA h $g^{-1}$ when the current density is restored to 0.1 A $g^{-1}$. This indicates that the unique multilevel carbon confinement of the ZCS@NC@C@rGO offers fast ion/electron transport channels, which effectively improves the rate performance of the electrode [41]. Fig. 4e, S5c and S5d show the charge/discharge curves of the ZCS@NC@C@rGO, ZCS@NC and ZCS@NC@C at different current densities. Clearly, the ZCS@NC@C@rGO possesses much better rate performance than the ZCS@NC and ZCS@NC@C. From Fig. 4f, S6 and Table S1, our proposed ZCS@NC@C@rGO anode exhibits excellent electrochemical properties, which is comparable to the recent reported anodes for PIBs [42–50]. The long-term cycling curves of the ZCS@NC, ZCS@NC@C and ZCS@NC@C@rGO at 2 A $g^{-1}$ are shown in Fig. 4g. As expected, the ZCS@NC@C@rGO anode still delivers a very high reversible specific capacity of 234 mA h $g^{-1}$ after 2000 cycles, whereas the specific capacities of ZCS@NC and ZCS@NC@C C anodes drop to 93.6 mA h $g^{-1}$ and 72.7 mA h $g^{-1}$ after 2000 cycles, respectively. Figure S7 also shows that the ZCS@NC@C@rGO basically maintains the micromorphology of micorcubes after the long-term cycles. Obviously, our designed multilevel carbon-confined micromorphology effectively mitigates volume expansion and reduces potassium storage stress as well as avoids

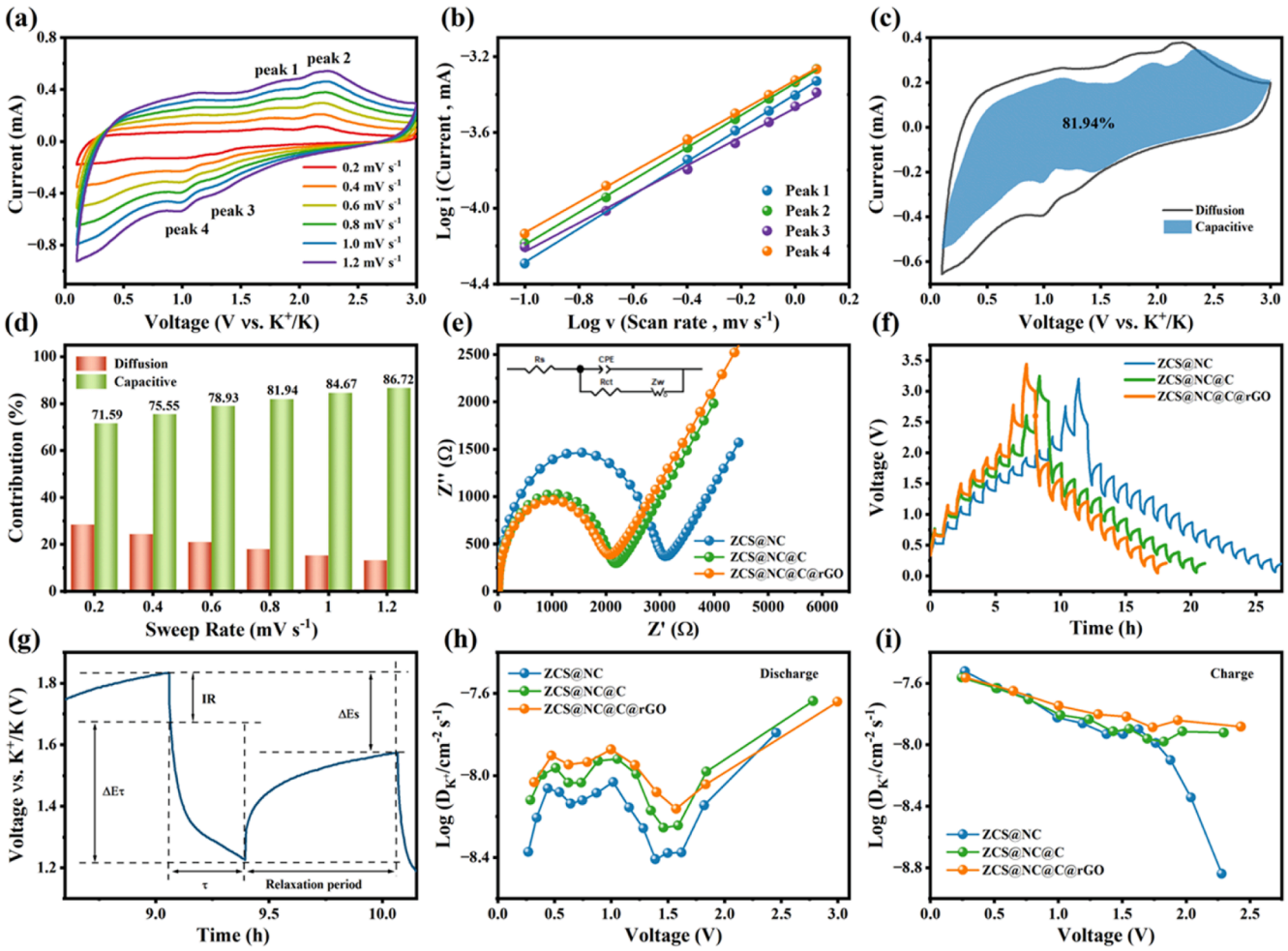


**Fig. 5.** (a) CV curves of ZCS@NC@C@rGO at different scan rates; (b) Relationship between log *v* and log *i* for ZCS@NC@C@rGO; (c) Capacitive contribution for ZCS@NC@C@rGO at 0.8 mV $s^{-1}$; (d) Percentages of capacitance-controlled behavior to the total capacity for ZCS@NC@C@rGO at various scan rates; (e) Nyquist plots for ZCS@NC, ZCS@NC@C and ZCS@NC@C@rGO electrodes; (f) GITT curves for ZCS@NC, ZCS@NC@C and ZCS@NC@C@rGO; (g) Detailed voltage response in a onefold current pulse process; $D_{K^+}$ in (h) discharge and (i) charge processes for ZCS@NC, ZCS@NC@C and ZCS@NC@C@rGO.

crushing and pulverization of the electrode, leading to excellent long cycle stability of the ZCS@NC@C@rGO. The outstanding electrochemical performance of the ZCS@NC@C@rGO is attributed to the synergistic effect of bimetallic selenides and the unique three-carbon confinement microstructure.

To evaluate the kinetic processes of the ZCS@NC, ZCS@NC@C and ZCS@NC@C@rGO anode, CV tests are performed at scan rates from 0.2 to 1.2 mV $s^{-1}$. As shown in Fig. 5a, the cathodic peaks of the ZCS@NC@C@rGO slightly shift towards low potentials, while the anodic peaks slightly shift towards high potentials with the increasing scan rate. The CV curves of the ZCS@NC and ZCS@NC@C at different sweep rates are shown in Figures S8a and S8b, respectively. In general, the equation $i = av^b$ is used to describe the relationship between the peak (i) and the scan rate (v), where the value of $a$ can be determined from the slope of the linear fit of log(i) and log(v) [51,52], and the value of $b$ implies the contribution of either the diffusion of $K^+$-ions (if $b = 0.5$) or the surface capacitance (if $b = 1.0$), respectively [53,54]. From the fitted curves in Fig. 5b, the values of $b$ associated to Peaks 1 to 4 of the CV curves are calculated as 0.887, 0.855, 0.758, and 0.805, respectively, indicating that the capacity of the ZCS@NC@C@rGO is jointly determined by the diffusion control process and the pseudocapacitive control process. According to the fitting curves in Figures S8c and S8d, the $b$ values of the ZCS@NC corresponding to the 1st to 4th peaks of CV curves are calculated to be 0.8224, 0.8289, 0.6583 and 0.674, respectively, while the $b$ values of the ZCS@NC@C are 0.8754, 0.8115, 0.6998 and 0.6612, respectively. The proportion of the pseudocapacitance contribution can be determined by the equation $i = k_1v + k_2v^{0.5}$ [55], where $k_1v$ and $k_2v^{0.5}$ represent the pseudocapacitance and diffusion control processes, respectively. By integrating the CV curves (Fig. 5c, and S9a and b), when the scan rate reaches 0.8 mV $s^{-1}$, the capacitance contribution accounts for 81.94% of the total capacity of the ZCS@NC@C@rGO. On the other hand, the capacitance contributions of the ZCS@NC and ZCS@NC@C only account for 38.56% and 77.66% of the total capacity, respectively, at the same scan rate. Clearly, the high pseudocapacitance contribution mainly originates from the multilevel carbons and the synergistic interaction between metallic selenides [56]. As shown in Fig. 5d, the capacitance contributions of the ZCS@NC@C@rGO are 71.6%, 75.6%, 78.9%, 81.9%, 84.7% and 86.7% at the scan rates of 0.2, 0.4, 0.6, 0.8, 1.0 and 1.2 mV $s^{-1}$, respectively, while Figure S9c and d show that the ZCS@NC@C possesses larger capacitive contributions than the ZCS@NC but lower contributions than the ZCS@NC@C@rGO at different scan rates. The great involvement in the capacitive behavior for the ZCS@NC@C@rGO can be attributed to the large surface area and abundant active sites in the triple-carbon spatial confined framework. The Nyquist plots for the ZCS@NC, ZCS@NC@C and ZCS@NC@C@rGO electrodes are shown in Fig. 5e, in which the interfacial resistance ($R_f$) and charge transfer resistance ($R_{ct}$) of the ZCS@NC@C@rGO are smaller than those of the ZCS@NC and ZCS@NC@C, indicating that the transport rate of potassium ions is faster in the ZCS@NC@C@rGO due to the high electronic conductivity

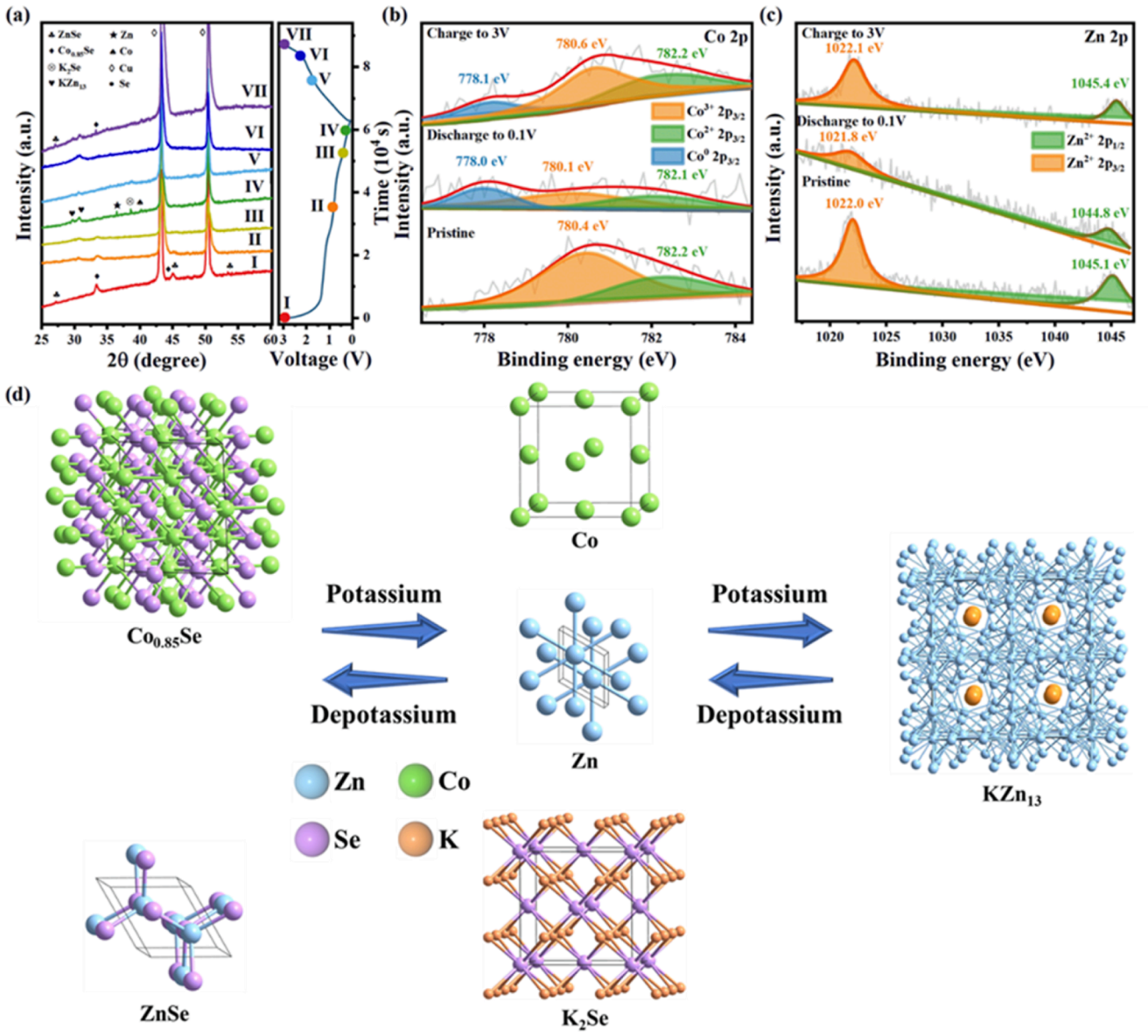


**Fig. 6.** (a) *Ex-situ* XRD patterns of ZCS@NC@C@rGO electrode at various charge-discharge states during the third charge-discharge process (I: initial state; II: discharged to 0.9 V; III discharged to 0.4 V; IV: discharged to 0.1 V; V: charged to 1.8 V; VI: charged to 2.2 V; VII: charged to 3 V); *Ex-situ* XPS spectra of (b) Co 2p and (c) Zn 2p at different charge/discharge states for ZSC@NC@C@rGO electrode; and (d) Potassium storage mechanism of ZCS@NC@C@rGO.

of the carbon layer and graphene, which greatly accelerates the electrochemical reaction kinetics. To further investigate the diffusion kinetics, the $K^+$ diffusion coefficients ($D_K^+$) of the ZCS@NC, ZCS@NC@C@rGO and ZCS@NC@C are determined by a constant current intermittent titration (GITT) technique using the following equation [57]:

$$D_{K^+} = \frac{4L^2}{\pi\tau}\left(\frac{\Delta E_S}{\Delta E_t}\right)^2 \quad (1)$$

where $\tau$ is the current pulse time (s), $\Delta E_S$ is the deviation of each equilibrium voltage, $\Delta E_t$ is the deviation voltage during the current pulse, and $L$ is the average thickness of electrode. Fig. 5f shows the GITT curves for the ZCS@NC and ZCS@NC@C and ZCS@NC@C@rGO in the voltage range of 0.1–3.0 V. As shown in Fig. 5g, the parameters used to calculate $D_K^+$ can be obtained from the single-step GITT measurements, and the corresponding values of $D_K^+$ for the discharge and charging processes are shown in Fig. 5h and 5i, respectively. Clearly, the $D_K^+$ values of the ZCS@NC@C@rGO are much higher than those of the ZCS@NC and ZCS@NC@C in both processes, indicating a faster electrochemical reaction kinetic behavior.

To further reveal the electrochemical mechanism of the potassification/depotassium process, the crystal structures of the ZCS@NC@C@rGO at different charge/discharge states are investigated by *ex-situ* XRD. As shown in Fig. 6a, in the initial state, four distinct peaks can be observed at 27.09, 45.03, 53.41, 33.33 and 44.95°, which are ascribed to the ZnSe ((1 1 1), (2 2 0) and (3 3 1) planes) and $Co_{0.85}Se$ ((1 0 1) and (1 0 2) planes), respectively. The characteristic peaks of ZnSe and $Co_{0.85}Se$ disappear when discharging to 0.9 V and 0.4 V. When discharged to 0.1 V, the diffraction peaks at 29.59, 30.42, 36.48, 38.62 and 40.34° are consistent with the characteristic diffraction peaks of (0 0 4) and (0 2 4) planes of $KZn_{13}$, (0 0 2) plane of Zn, (3 1 1) plane of $K_2Se$ and (1 0 0) plane of Co, respectively. The disappearance of the $Co_{0.85}Se$ peak indicates that the $Co_{0.85}Se$ has been converted to Co and $K_2Se$, meanwhile, the disappearance of the ZnSe peak indicates that the conversion reaction has occurred before the alloying reaction to form $KZn_{13}$ and $K_2Se$. When charged to 2.2 V, the diffraction peak of $K_2Se$ disappears, indicating that the conversion-alloy reaction occurs between

1.8 and 2.2 V. At a full charge of 3 V, the diffraction peaks correspond to $Co_{0.85}Se$ (JCPDS No. 52–1008) and ZnSe (JCPDS No. 37-1463), respectively. It should be noted that the diffraction peaks are similar when discharged to 0.9 V/charged to 2.2 V and discharged to 0.4 V/charged to 1.8 V, indicating the high reversibility of the insertion and de-insertion reactions of $K^+$. To further understand the reaction mechanism, we perform *ex-situ* XPS tests on the ZCS@NC@C@rGO. Fig. 6b shows the high-resolution Co 2p XPS spectra at different charging and discharging states. The peaks of $Co^{3+}$ $2p_{3/2}$ and $Co^{2+}$ $2p_{3/2}$ gradually diminish as the discharge proceeds, and the peak of $Co^0$ $2p_{3/2}$ appears at 778.0 eV when discharged to 0.1 V, indicating the reduction of $Co_{0.85}Se$ to Co metal during the insertion of $K^+$. As the charging process proceeds, the peak of $Co^0$ $2p_{3/2}$ gradually diminishes, and when charged to 3.0 V, the peaks of $Co^{3+}$ $2p_{3/2}$ and $Co^{2+}$ $2p_{3/2}$ are almost identical to the original state, corresponding to the Co in $Co_{0.85}Se$. Fig. 6c shows the high-resolution Zn 2p XPS spectra at different charging and discharging states. In the initial state, two main peaks are observed at 1022.0 eV and 1045.1 eV, corresponding to Zn $2p_{3/2}$ and Zn $2p_{1/2}$, respectively. When discharged to 0.1 V, Zn $2p_{3/2}$ (1021.8 eV) and Zn $2p_{1/2}$ (1044.8 eV) are the two main peaks attributed to the fully potassiumized state of the metal, indicating that the conversion-alloying reaction from $Zn^{2+}$ to the $KZn_{13}$ alloy has occurred. When charged to 3.0 V, i.e., complete depotassium, the peaks of Zn $2p_{3/2}$ and Zn $2p_{1/2}$ are almost identical to their original states, corresponding to the Zn in the ZnSe. Fig. 6d shows the mechanism of a reversible conversion-alloying reaction of the active material of ZnSe/$Co_{0.85}Se$ during potassium storage, which can be described as:

$$ZnSe + 2K^+ + 2e^- \leftrightarrow Zn + K_2Se \quad (2)$$

$$13Zn + K^+ + e^- \leftrightarrow KZn_{13} \quad (3)$$

$$Co_{0.85}Se + 2K^+ + 2e^- \leftrightarrow 0.85Co + K_2Se \quad (4)$$

The results indicate that the high capacity of the conversion-alloying reaction and the more active centers provided by the bimetallic selenide favor the efficient and reversible potassium storage process in the ZCS@NC@C@rGO.

## 3. Conclusion

In summary, we have proposed a multilevel spatial confinement strategy for the synthesis of high-performance anodes (ZnSe/$Co_{0.85}Se$@NC@C@rGO) for PIBs by *in-situ* carbonization and selenization of RF-coated ZIF-8/ZIF-67 encapsulated into two-dimensional graphene. The micromorphology of 3D interconnected carbon network embedded with bimetallic selenides exhibits the unique advantages: (1) the porous carbon microcubes and carbon shell provide rich channels for ion/electron transfer and space with a certain volume margin for alleviating the effects of volume change and inhibiting the agglomeration of active material, and present a rigid skeleton to ensure the structural stability of the material, and (2) the 3D carbon network enhances the electron/ion transfer rate and electrochemical reaction kinetics of the material. Due to the efficient multilevel spatial carbon confinement, the ZnSe/$Co_{0.85}Se$@NC@C@rGO possesses the excellent potassium storage performance: a good rate performance of 203.9 mA h $g^{-1}$ at 5 A $g^{-1}$ and a brilliant long-term cycling performance of 234 mA h $g^{-1}$ after 2000 cycles. The investigations on *ex-situ* XRD and XPS of the material reveals that the intercalation/de-intercalation of $K^+$ proceeds through the conversion-alloying reaction. The present work opens up a new path for the rational construction of advanced anodes for PIBs and provides new insights into the storage mechanism of $K^+$ for transition metal selenides.

### *CRediT authorship contribution statement*

**Rui Zhang:** Methodology, Writing – original draft. **Qing Luo:** Methodology, Writing – original draft. **Juan Gong:** Formal analysis. **Zhikun Chen:** Investigation. **Zhuang Wu:** Investigation. **Shiman Li:** Resources. **Qiaoji Zheng:** Conceptualization, Supervision. **Xiaochun Wu:** Supervision. **Kwok-ho Lam:** Conceptualization, Writing – review & editing. **Dunmin Lin:** Conceptualization, Writing – review & editing.

### Declaration of Competing Interest

The authors declare the following financial interests/personal relationships which may be considered as potential competing interests: Rui Zhang reports financial support was provided by National College Students' innovation and entrepreneurship training program. Dunmin Lin reports financial support was provided by Natural Science Foundation of Sichuan Province. Dunmin Lin reports financial support was provided by Sichuan Province Science and Technology Support Program.

### Data availability

Data will be made available on request.

### Acknowledgements

This work was supported by National College Students' innovation and entrepreneurship training program (202110636001), Natural Science Foundation of Sichuan Province (2022NSFSC0222), Sichuan Science and Technology Program (2023NSFSC0439) and partially by the University of Glasgow.

### Appendix A. Supplementary data

Supplementary data to this article can be found online at https://doi.org/10.1016/j.jcis.2023.04.035.

### References

[1] J.W. Choi, D. Aurbach, Promise and reality of post-lithium-ion batteries with high energy densities, Nat. Rev. Mater. 1 (2016) 16013.
[2] C.P. Grey, J.M. Tarascon, Sustainability and in situ monitoring in battery development, Nat. Mater. 16 (2017) 45–56.
[3] Y. Liu, Z. Tai, J. Zhang, W.K. Pang, Q. Zhang, H. Feng, K. Konstantinov, Z. Guo, H. K. Liu, Boosting potassium-ion batteries by few-layered composite anodes prepared via solution-triggered one-step shear exfoliation, Nat. Commun. 9 (2018) 3645.
[4] J. Yang, Z. Ju, Y. Jiang, Z. Xing, B. Xi, J. Feng, S. Xiong, Enhanced capacity and rate capability of nitrogen/oxygen dual-doped hard carbon in capacitive potassium-ion storage, Adv. Mater. 30 (2017) 1700104.
[5] Q. Zhang, J. Mao, W.K. Pang, T. Zheng, V. Sencadas, Y. Chen, Y. Liu, Z. Guo, Boosting the potassium storage performance of alloy-based anode materials via electrolyte salt chemistry, Adv. Energy Mater. 8 (2018) 1703288.
[6] S. Chong, Y. Wu, C. Liu, Y. Chen, S. Guo, Y. Liu, G. Cao, Cryptomelane-type $MnO_2$/carbon nanotube hybrids as bifunctional electrode material for high capacity potassium-ion full batteries, Nano Energy 54 (2018) 106–115.
[7] D.-S. Bin, X.-J. Lin, Y.-G. Sun, Y.-S. Xu, K. Zhang, A.-M. Cao, L.-J. Wan, Engineering hollow carbon architecture for high-performance K-ion battery anode, J. Am. Chem. Soc. 140 (2018) 7127–7134.
[8] J. Ge, L. Fan, J. Wang, Q. Zhang, Z. Liu, E. Zhang, Q. Liu, X. Yu, B. Lu, $MoSe_2$/N-doped carbon as anodes for potassium-ion batteries, Adv. Energy Mater. 8 (2018) 1801477.
[9] L. Li, L. Liu, Z. Hu, Y. Lu, Q. Liu, S. Jin, Q. Zhang, S. Zhao, S.-L. Chou, Understanding high-rate $K^+$-solvent co-intercalation in natural graphite for potassium-ion batteries, Angew. Chem. Int. Edit 59 (2020) 12917–12924.
[10] X. Wei, J. Wei, Y. Song, D. Wu, X.D. Liu, H. Chen, P. Xiao, Y. Zhang, Potassium mediated Co-Fe-based Prussian blue analogue architectures for aqueous potassium-ion storage, Chem. Commun. 57 (2021) 7019–7022.
[11] L. Xu, W. Guo, L. Zeng, X. Xia, Y. Wang, P. Xiong, Q. Chen, J. Zhang, M. Wei, Q. Qian, $V_3Se_4$ embedded within N/P co-doped carbon fibers for sodium/potassium ion batteries, Chem. Eng. J. 419 (2021), 129607.
[12] Q. Peng, F. Ling, H. Yang, P. Duan, R. Xu, Q. Wang, Y. Yu, Boosting potassium storage performance via construction of $NbSe_2$-based misfit layered chalcogenides, Energy Storage Mater. 39 (2021) 265–270.
[13] W. Zhao, X. Xu, L. Wang, Y. Liu, T. Zhou, S. Zhang, J. Hu, Q. Jiang, Boosting lifespan of conversion-reaction anodes for full/half potassium-ion batteries via multi-dimensional carbon nano-architectures confinement effect, J. Energy Chem. 75 (2022) 55–65.

[14] Y. Liu, Q. Wan, J. Gong, Z. Liu, G. Tao, J. Zhao, L. Chen, W. Li, X. Wei, L. Ni, Y. Song, Confine, defect, and interface manipulation of $Fe_3Se_4$/3D graphene targeting fast and stable potassium-ion storage, Small 19 (2022) 2206400.

[15] Q. Yu, B. Jiang, J. Hu, C.-Y. Lao, Y. Gao, P. Li, Z. Liu, G. Suo, D. He, W.A. Wang, G. Yin, Metallic octahedral $CoSe_2$ threaded by N-doped carbon nanotubes: a flexible framework for high-performance potassium-ion batteries, Adv. Sci. 5 (2018) 1800782.

[16] J. Wang, B. Wang, X. Liu, J. Bai, H. Wang, G. Wang, Prussian blue analogs (PBA) derived porous bimetal (Mn, Fe) selenide with carbon nanotubes as anode materials for sodium and potassium ion batteries, Chem. Eng. J. 382 (2019), 123050.

[17] Q. Li, H. Liu, Z. Yao, C. Wolverton, J. Wu, V.P. Dravid, Kinetics of sodium and selenium reactions in sodium ion batteries, Microsc. Microanal. 22 (2016) 826–829.

[18] F. Wang, Y. Liu, H.-J. Wei, T.-F. Li, X.-H. Xiong, S.-Z. Wei, F.-Z. Ren, A.A. Volinsky, Recent advances and perspective in metal coordination materials-based electrode materials for potassium-ion batteries, Rare Met. 40 (2021) 448–470.

[19] Y. Du, Z. Zhang, Y. Xu, J. Bao, X. Zhou, Metal sulfide-based potassium-ion battery anodes: storage mechanisms and synthesis strategies, Acta Phys.-Chim. Sin. 38 (2022) 2205017.

[20] C. Hu, K. Ma, Y. Hu, A. Chen, P. Saha, H. Jiang, C. Li, Confining $MoS_2$ nanocrystals in MOF-derived carbon for high performance lithium and potassium storage, Green Energy Environ. 6 (2021) 75–82.

[21] X. Xu, J. Liu, Z. Liu, J. Shen, R. Hu, J. Liu, L. Ouyang, L. Zhang, M. Zhu, Robust pitaya-structured pyrite as high energy density cathode for high-rate lithium batteries, ACS Nano 9 (2017) 9033–9040.

[22] K. Han, Z. Liu, P. Li, Q. Yu, W. Wang, C.-Y. Lao, D. He, W. Zhao, G. Suo, H. Guo, L. Song, M. Qin, X. Qu, High-throughput fabrication of 3D N-doped graphenic framework coupled with $Fe_3C$@porous graphite carbon for ultrastable potassium ion storage, Energy Storage Mater. 22 (2019) 185–193.

[23] X. Wei, B. Liu, Z. Chen, K. Wu, Y. Liu, X. Yuan, X. Zhang, X. Liu, Q. Wan, Y. Song, Recent advances in modulation engineering-enabled metal compounds for potassium-ion storage, Energy Storage Mater. 51 (2022) 815–839.

[24] G. Yang, C. Yan, P. Hu, Q. Fu, H. Zhao, Y. Lei, Synthesis of $CoSe_2$ reinforced nitrogen-doped carbon composites as advanced anodes for potassium-ion batteries, Inorg. Chem. Front. 9 (2022) 3719–3727.

[25] X. Jia, E. Zhang, X. Yu, B. Lu, Facile synthesis of copper sulfide nanosheet@graphene oxide for the anode of potassium-ion batteries, Energy Technol. 8 (2019) 1900987.

[26] Z. Meng, Z. Qiu, Y. Shi, S. Wang, G. Zhang, Y. Pi, H. Pang, Micro/nano metal-organic frameworks meet energy chemistry: a review of materials synthesis and applications, eScience (2023) 100092.

[27] M. Huang, K. Mi, J. Zhang, H. Liu, T. Yu, A. Yuan, Q. Kong, S. Xiong, MOF-derived bi-metal embedded N-doped carbon polyhedral nanocages with enhanced lithium storage, J. Mater. Chem. A 5 (2016) 266–274.

[28] Y. Ouyang, X. Xia, H. Ye, L. Wang, X. Jiao, W. Lei, Q. Hao, Three-dimensional hierarchical structure ZnO@C@NiO on carbon cloth for asymmetric supercapacitor with enhanced cycle stability, ACS Appl. Mater. Interfaces 10 (2018) 3549–3561.

[29] H. Wang, X. Wang, D. Yang, B. Zheng, Y. Chen, $Co_{0.85}Se$ hollow nanospheres anchored on N-doped graphene nanosheets as highly efficient, nonprecious electrocatalyst for hydrogen evolution reaction in both acid and alkaline media, J. Power Sources 400 (2018) 232–241.

[30] W. Ding, S. Wang, X. Wu, Y. Wang, Y. Li, P. Zhou, T. Zhou, J. Zhou, S. Zhuo, $Co_{0.85}Se$@C/$Ti_3C_2T_x$ MXene hybrids as anode materials for lithium-ion batteries, J. Alloys Compd. 816 (2020), 152566.

[31] H. Liu, H. Guo, B. Liu, M. Liang, Z. Lv, K.R. Adair, X. Sun, Few-layer $MoSe_2$ nanosheets with expanded (002) planes confined in hollow carbon nanospheres for ultrahigh-performance Na-ion batteries, Adv. Funct. Mater. 28 (2018) 1707480.

[32] G. Zhang, K. Liu, S. Liu, H. Song, J. Zhou, Flexible $Co_{0.85}Se$ nanosheets/graphene composite film as binder-free anode with high Li- and Na-Ion storage performance, J. Alloys Compd. 731 (2018) 714–722.

[33] Z. Zhang, Y. Huang, X. Liu, X. Wang, P. Liu, Core-Shell Co, Zn Bimetallic selenide embedded nitrogen-doped carbon polyhedral frameworks assist in sodium-ion battery ultralong cycle, ACS Sustainable Chem. Eng. 8 (2020) 8381–8390.

[34] S.-K. Park, Y.C. Kang, MOF-templated N-doped carbon-coated $CoSe_2$ nanorods supported on porous CNT microspheres with excellent sodium-ion storage and electrocatalytic properties, ACS Appl. Mater. Interfaces 10 (2018) 17203–17213.

[35] C. Atangana Etogo, H. Huang, H. Hong, G. Liu, L. Zhang, Metal-organic-frameworks-engaged formation of $Co_{0.85}Se$@C nanoboxes embedded in carbon nanofibers film for enhanced potassium-ion storage, Energy Storage Mater. 24 (2019) 167–176.

[36] J. Yang, H. Gao, S. Men, Z. Shi, Z. Lin, X. Kang, S. Chen, $CoSe_2$ Nanoparticles encapsulated by N-doped carbon framework intertwined with carbon nanotubes: high-performance dual-role anode materials for both Li- and Na-ion batteries, Adv. Sci. 5 (2018) 1800763.

[37] X.M. Lin, J.H. Chen, J.J. Fan, Y. Ma, P. Radjenovic, Q.C. Xu, L. Huang, S. Passerini, Z.Q. Tian, J.F. Li, Synthesis and operando sodiation mechanistic study of nitrogen-doped porous carbon coated bimetallic sulfide hollow nanocubes as advanced sodium ion battery anode, Adv. Energy Mater. 9 (2019) 1902312.

[38] S. Lu, T. Zhu, H. Wu, Y. Wang, J. Li, A. Abdelkader, K. Xi, W. Wang, Y. Li, S. Ding, G. Gao, R.V. Kumar, Construction of ultrafine ZnSe nanoparticles on/in amorphous carbon hollow nanospheres with high-power-density sodium storage, Nano Energy 59 (2019) 762–772.

[39] Y. He, L. Wang, C. Dong, C. Li, X. Ding, Y. Qian, L. Xu, In-situ rooting ZnSe/N-doped hollow carbon architectures as high-rate and long-life anode materials for half/full sodium-ion and potassium-ion batteries, Energy Storage Mater. 23 (2019) 35–45.

[40] C. Dong, L. Wu, Y. He, Y. Zhou, X. Sun, W. Du, X. Sun, L. Xu, F. Jiang, Willow-leaf-like ZnSe@N-doped carbon nanoarchitecture as a stable and high-performance anode material for sodium-ion and potassium-ion batteries, Small 16 (2020) 2004580.

[41] X.-X. Jia, X.-Z. Yu, B.-A. Lu, $Fe_{0.8}CoSe_2$ nanosphere coated by N-doped carbon for ultra-high rate potassium selenium battery, Rare Met. 40 (2021) 2455–2463.

[42] J. Chen, Y. Cheng, Q. Zhang, C. Luo, H.Y. Li, Y. Wu, H. Zhang, X. Wang, H. Liu, X. He, J. Han, D.L. Peng, M. Liu, M.S. Wang, Designing and understanding the superior potassium storage performance of nitrogen/phosphorus co-doped hollow porous bowl-like carbon anodes, Adv. Funct. Mater. 31 (2020) 2007158.

[43] X. Sui, X. Huang, H. Pu, Y. Wang, J. Chen, Tailoring MOF-derived porous carbon nanorods confined red phosphorous for superior potassium-ion storage, Nano Energy 83 (2021), 105797.

[44] C. Zhang, H. Li, X. Zeng, S. Xi, R. Wang, L. Zhang, G. Liang, K. Davey, Y. Liu, L. Zhang, S. Zhang, Z. Guo, Accelerated diffusion kinetics in ZnTe/$CoTe_2$ heterojunctions for high rate potassium storage, Adv. Energy Mater. 12 (2022) 2202577.

[45] Y. Liu, Q. Deng, Y. Li, Y. Li, W. Zhong, J. Hu, X. Ji, C. Yang, Z. Lin, K. Huang, CoSe@N-doped carbon nanotubes as a potassium-ion battery anode with high initial coulombic efficiency and superior capacity retention, ACS Nano 15 (2021) 1121–1132.

[46] F. Qiao, J. Wang, Y. Zhu, X. Tan, X. Wang, Q. An, Cheese-like porous $SnP_2O_7$ composite as a long-life and high-rate anode material for potassium-ion batteries, Chem. Eng. J. 439 (2022), 135777.

[47] H. Shan, J. Qin, Y. Ding, H.M.K. Sari, X. Song, W. Liu, Y. Hao, J. Wang, C. Xie, J. Zhang, X. Li, Controllable heterojunctions with a semicoherent phase boundary boosting the potassium storage of $CoSe_2$/$FeSe_2$, Adv. Mater. 33 (2021) 2102471.

[48] Y. Chen, X. Shi, B. Lu, J. Zhou, Concave engineering of hollow carbon spheres toward advanced anode material for sodium/potassium-ion batteries, Adv. Energy Mater. 12 (2022) 2202851.

[49] Z. Wu, G. Liang, J. Wu, W.K. Pang, F. Yang, L. Chen, B. Johannessen, Z. Guo, Synchrotron x-Ray absorption spectroscopy and electrochemical study of $Bi_2O_2Se$ electrode for lithium-/potassium-ion storage, Adv. Energy Mater. 11 (2021) 2100185.

[50] Y. Cao, Y. Zhang, H. Chen, S. Qin, L. Zhang, S. Guo, H. Yang, $Cu_{12}Sb_4S_{13}$ Quantum dots/few-layered $Ti_3C_2$ nanosheets with enhanced $K^+$ diffusion dynamics for efficient potassium ion storage, Adv. Funct. Mater. 32 (2021) 2108574.

[51] Z. Yi, Y. Qian, S. Jiang, Y. Li, N. Lin, Y. Qian, Self-wrinkled graphene as a mechanical buffer: A rational design to boost the K-ion storage performance of $Sb_2Se_3$ nanoparticles, Chem. Eng. J. 379 (2019), 122352.

[52] W. Luo, F. Li, W. Zhang, K. Han, J.-J. Gaumet, H.-E. Schaefer, L. Mai, Encapsulating segment-like antimony nanorod in hollow carbon tube as long-lifespan, high-rate anodes for rechargeable K-ion batteries, Nano Res. 12 (2019) 1025–1031.

[53] J. Xie, Y. Zhu, N. Zhuang, H. Lei, W. Zhu, Y. Fu, M.S. Javed, J. Li, W. Mai, Rational design of metal organic framework-derived $FeS_2$ hollow nanocages@reduced graphene oxide for K-ion storage, Nanoscale 10 (2018) 17092–17098.

[54] Z. Liu, P. Li, G. Suo, S. Gong, W. Wang, C.-Y. Lao, Y. Xie, H. Guo, Q. Yu, W. Zhao, K. Han, Q. Wang, M. Qin, K. Xi, X. Qu, Zero-strain $K_{0.6}Mn_1F_{2.7}$ hollow nanocubes for ultrastable potassium ion storage, Energy Environ. Sci. 11 (2018) 3033–3042.

[55] H. Wu, Q. Yu, C.-Y. Lao, M. Qin, W. Wang, Z. Liu, C. Man, L. Wang, B. Jia, X. Qu, Scalable synthesis of VN quantum dots encapsulated in ultralarge pillared N-doped mesoporous carbon microsheets for superior potassium storage, Energy Storage Mater. 18 (2018) 43–50.

[56] F. Yuan, Y.-C. Shao, B. Wang, Y.-S. Wu, D. Zhang, Z.-J. Li Y.-m.A., Wu, Recent progress in application of cobalt-based compounds as anode materials for high-performance potassium-ion batteries, Rare Met. 41 (2022) 3301–3321.

[57] S. Dong, D. Yu, J. Yang, L. Jiang, J. Wang, L. Cheng, Y. Zhou, H. Yue, H. Wang, L. Guo, Tellurium: a high-volumetric-capacity potassium-ion battery electrode material, Adv. Mater. 32 (2020) 1908027.